Extension of Kelvin's equation to dipolar colloids

Kedar Joshi[a] and Sibani Lisa Biswal[a,1]

[a]Department of Chemical and Biomolecular Engineering, Rice University, Houston, TX 77005

Vapor pressure refers to the pressure exerted by the vapor phase in thermodynamic equilibrium with either its liquid or solid phase. An important class of active matter is field-driven colloids. A suspension of dipolar colloids placed in a high-frequency rotating magnetic field undergoes a nonequilibrium phase transition into a dilute and dense phase, akin to liquid–vapor coexistence in a simple fluid. Here, we compute the vapor pressure of this colloidal fluid. The number of particles that exist as the dilute bulk phase versus condensed cluster phases can be directly visualized. An exponential relationship between vapor pressure and effective temperature is determined as a function of applied field strength, analogous to the thermodynamic expression between vapor pressure and temperature found for pure liquids. Additionally, we demonstrate the applicability of Kelvin's equation to this field-driven system. In principle, this appears to be in conflict with macroscopic thermodynamic assumptions due to the nonequilibrium and discrete nature of this colloidal system. However, the curvature of the vapor–liquid interface provides a mechanical equilibrium characterized by interfacial tension that connects the condensed clusters observed with these active fluids to classical colligative fluid properties.

magnetic colloids | nonequilibrium | statistical thermodynamics | vapor pressure

Colloidal systems have long been used as model systems to understand the dynamics and physical properties of molecular systems. Millimeter-sized colloids exhibit Brownian motion, whereby a suspension can be described by using statistical mechanics to answer questions relevant to many areas of condensed- and soft-matter science. Field-driven and active colloids are out-of-equilibrium systems, yet demonstrate a host of emergent collective behavior (1–4), including self-assembled swimmers (5–7), microbots (8–11), and fluid-like fronts (12, 13). Additionally, these "big atoms" demonstrate crystallization, condensations, and phase separation, mirroring molecular equilibrium phenomena (14–17). Tunable interactions have allowed for a detailed understanding of the nucleation and melting dynamics (18, 19), which is important in understanding the properties of various two-dimensional (2D) functional materials, such as graphene, protein membranes, and polymer thin films (20–22). Phase transitions are important in equilibrium systems, and analogous phenomena play an equally important role in the organization of nonequilibrium systems (23). Externally applied fields can be used to generate a long-range attractive interaction potential that is tunable (24–34). Vapor–liquid–solid transitions can be directed by modulating field strength and frequency. Although these colloidal dynamics are inherently nonequilibrium, the result is an interaction potential that mimics an effective temperature (35, 36) or pressure (37, 38). It has been shown that dilute vapor coexists with dense liquid colloidal clusters, and crystals exhibit properties such as line tension (39–41), spinodal phases (42, 43), and energy dissipation (44), characteristic of molecular systems. Generalized thermodynamic concepts such as free energy, surface tension, and classical nucleation theory have also been applied to active colloidal systems (45–47). Concepts such as swim pressure have been used to describe motility-induced phase separation of systems that exhibit propulsion (48–53). However, it remains unclear

to what extent thermodynamic concepts can be extended to nonequilibrium systems. Vapor pressure is one such colligative property of interest. It is defined as the pressure exerted by a vapor phase in equilibrium with its condensed liquid phase. In classical thermodynamics, vapor pressure is a continuous property that depends on the temperature and average size of liquid droplets (54). The very nature of this equilibrium constitutes balancing the rate of exchange of molecules between the vapor and liquid phases. Here, we characterize the vapor–liquid coexistence of dipolar colloids by using the lever rule to quantify the relative composition of particles in each phase and Kelvin's equation to calculate the "effective" vapor pressure. Our investigation builds upon our previous work, in which a rotating magnetic field (RMF) is used to induce phase separation with spatiotemporal scaling laws that depend on the volume fraction of particles and applied field strength (42). From thermodynamics, the vapor phase constantly exerts an osmotic pressure onto the liquid phase, which is defined as vapor pressure. We conjecture that our particle-dilute phase also exerts an osmotic pressure on the cluster phase, which is balanced by the time-averaged dipolar interactions.

Results and Discussion

Our experiments used a suspension of 1.07-μm superparamagnetic spheres (Dynabeads MyOne Carboxylic Acid, Invitrogen) in a 10 mM NaCl solution sandwiched between parallel glass plates. The concentration of the particles ranged from 0.08 to

Significance

Suspensions of colloids driven out-of-equilibrium demonstrate interesting collective behavior, such as organized and directed clustering and swarming. These systems require continuous energy input, yet some of the dynamics of these driven systems resemble the equilibrium-phase behavior of molecular fluids, such as crystallization, condensation, and phase separation. Consequently, there has been significant interest in exploring the applicability of thermodynamic concepts, such as pressure and surface tension, to describe nonequilibrium phenomena. Here, we show how rotating magnetic fields can drive superparamagnetic particles to form steady-state vapor–liquid coexistence that can be analyzed with Kelvin's equation to determine an "effective vapor pressure" for this active colloidal system. These results illustrate the convergence of statistical physics of simple liquids to nonequilibrium colloidal fluids.

[1]To whom correspondence may be addressed. Email: biswal@rice.edu.

ENGINEERING

0.15 wt.%. An RMF with a fixed frequency of 20 Hz was applied with a field strength between 8 and 10.5 Gauss (G). The induced magnetic interaction potential between two particles, U_{mag}, in the presence of RMF, is given as $U_{mag} = -(m^2\alpha)/(\mu_o r^2)$, where r is the interparticle spacing, μ_o is the magnetic permeability of the medium, and α is a constant that depends on the geometric and material properties, as defined by Du et al. (55). Also, m is the magnitude of the induced dipole, $m = \chi_{eff} V_p B$, where $\chi_{eff} = 3\chi/(3 + \chi)$ is the effective magnetic susceptibility, V_p is the particle volume, and B is the magnetic field strength. Furthermore, the particles have a zeta potential of −50 mV, resulting in electrostatic repulsion.

A feature common to self-assembled systems is that the minimum potential energy determines the thermodynamically stable configuration. Our colloids organize via a dissipative assembly process, which requires a continuous input of energy (56). The fast rotating in-plane magnetic field leads to a dimensionless interaction energy, U_{pair}/kT, governed by a short-ranged repulsion and a long-ranged dipolar attraction, as shown in Fig. 1A. The minimum in this pairwise interaction potential, U_{min}/kT, was determined experimentally to decrease linearly as $1/B^2$ with a proportionality constant of −0.022, as shown by Fig. 1A, Inset. We define an effective temperature for our colloidal system: $T^* = kT/U_{min}$ or, correspondingly, $1/T^* \sim -0.022B^2$.

Transition Between Bulk (Vapor) to Coexistence with Liquid-Like Clusters. There have been a number of theoretical and simulations of 2D fluids with attractive Lennard–Jones-like interactions (57–59), but experiments that capture the coarsening dynamics are limited. Recent studies using RMF have characterized the phase behavior as a function of the magnetic field and particle concentration as particles (26, 28, 29, 60). The strength of the magnetic field, kT/U_{pair}, acts as an effective temperature, T^*, shown by characteristic vapor, liquid, and crystalline phases that arise with increasing magnetic field strength, which we have previously experimentally verified (42). Fig. 1B shows a simplified phase diagram as a function of B and particle volume fraction, ϕ, which is calibrated for a given suspension concentration. Kryuchkov et al. (29) have reported Monte Carlo simulations that identify the phase boundaries for this system, shown by the dashed lines on the phase diagram.

Here, our interest is the vapor–liquid coexistence. The points plotted on the phase diagram illustrate the experimental test conditions, where the range of applied magnetic field strengths varied from 8 to 10.5 G and particle density between 0.12 and 0.24. This corresponds to U_{min}/kT values between $1.4kT - 2.4kT$. Tracking of individual particle positions was conducted by using optical microscopy. Observations of a representative sample of the bulk particle distribution in the absence of an applied field is shown in Fig. 1C. Application of an RMF of 9 G ($U_{min}/kT = 1.8$) resulted in particles condensing into a liquid-like cluster in equilibrium with the dilute bulk phase, as shown in Fig. 1D. We have previously extracted the pair-correlation function and equilibrium structure factor to show that the clusters are disordered for these experimental conditions (39).
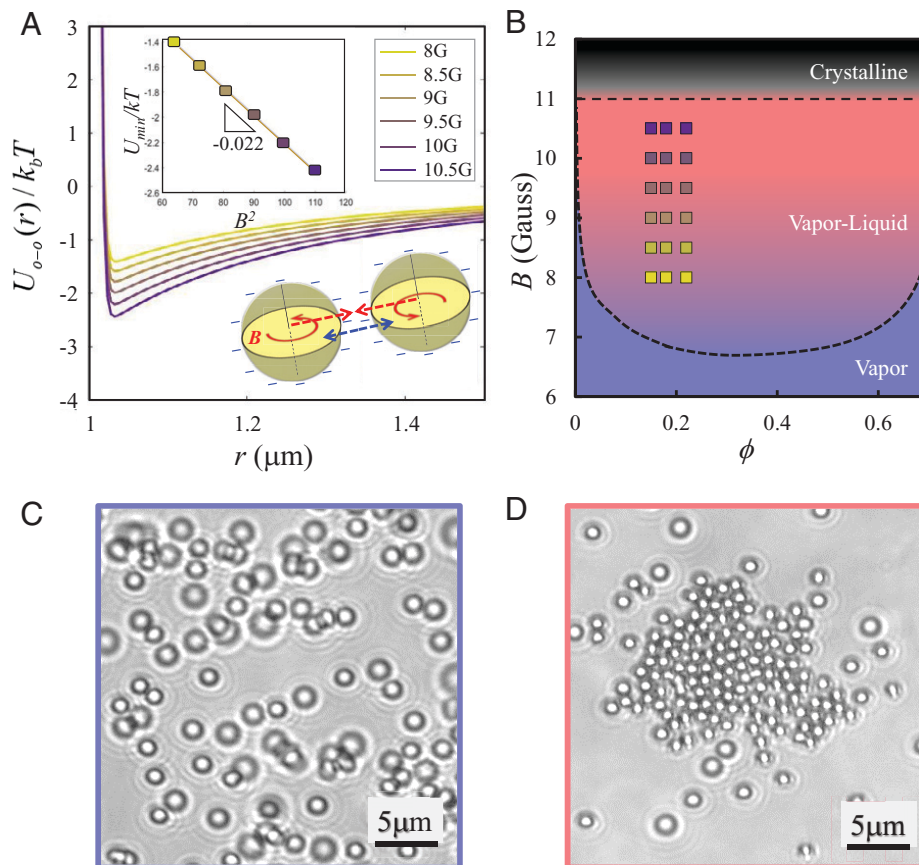

Fig. 1. (A) Particle pair potential, U_{o-o}, normalized by thermal fluctuation energy, kT, as a function of separation distance, r (the magnetic field is varied from 8 to 10.5 G). Inset shows U_{min}, normalized by kT as a function of B^2. The U_{min} shows a linear trend with B^2. (B) Phase transformation of the system of 1-μm paramagnetic colloids as a function of the strength of field and particle density under RMF. Bulk (vapor) to bulk–cluster (vapor–liquid) to crystalline (solid) transition is shown. As studied previously, the bold dashed black line (29, 42) indicates transition into the bulk–cluster coexistance region, and the upper dashed black line (19) at 11 G shows transition into a crystalline phase. All tested experimental conditions are located under the bulk–cluster coexistence curve. (C) Absence of RMF (vapor-like). (D) Nine Gauss (vapor–liquid coexistence).

The dynamics of the system are such that when the RMF is applied, nucleation and growth of clusters occur on the timescale of minutes. These clusters continue to grow and coarsen to reduce the total interfacial length of the system over several hours. Fig. 2A illustrates the phase separation over 3 h with an RMF of 8 G. Detailed phase identification using a Voronoi-based decomposition has been reported for colloidal systems with density distribution (61). Here, we identify the number of particles in the bulk (vapor) and average cluster size (liquid), as described in *Materials and Methods*. Fig. 2B shows how the average cluster size, R, normalized by the particle diameter, d, changes over time. The highlighted section in Fig. 2 B, *Inset* shows the nucleation of particle aggregates, but they are unstable and constantly appear and disappear. Once the cluster reaches a minimum size of $R_{min} \sim 4d$, cluster growth and coarsening occur. The coarsening dynamics follow a growth rate of $\sim t^{0.26}$. For the tested conditions reported, the coarsening process is over hours (slow). Although the clusters merge and coarsen, a quasi-equilibrium between particles in bulk and cluster phases is established. Evidence for quasi-equilibrium comes from measurements of the number density of particles for each phase.

Fig. 2C shows how the number of particles in bulk, N_B, reaches equilibrium within minutes when the RMF is changed from 9 to 8.5 G. Note that for a 2D system, the particle density is equivalent to an area fraction. Furthermore, $\partial R/\partial t$ is small for our test conditions, which suggests that the average cluster size and curvature do not change significantly. It is important to note that quasi-equilibrium occurs at our test conditions and would not easily occur at higher ϕ and B, where the dynamics are such that particle densities may not be constant within a given phase.

Cluster and Effective Vapor Pressure. At thermal equilibrium, the chemical potential between coexisting phases must be equal. For colloids at an effective temperature, T^*, equilibrium between the colloidal bulk and cluster phases can be defined by a Boltzmann distribution:

$$\phi_B = \phi_C \exp\left(\frac{\Delta\mu}{kT}\right), \qquad [1]$$

where ϕ_B and ϕ_C are the bulk and cluster particle densities, respectively; $\Delta\mu$ is the chemical potential difference between two pure phases; and kT is the product of the Boltzmann constant and temperature, also known as the thermal energy. For a discrete system, the chemical potential difference can also be defined as the change in Gibbs free energy divided by the change in the number of particles, $\Delta\mu = \Delta G/\Delta N_C$, where N_C is the average number of particles inside clusters.

For a 2D system, the pressure-equivalent term can be found by using the ideal gas equation of state, $pV = nkT$. For bulk–cluster coexistence, this pressure will be the equivalent vapor pressure of the system, P_V, with units of (J/m^2), which can be expressed as $P_V A_B = N_B kT$, where A_B is the bulk phase area. However, the bulk particle density, ϕ_B, is given as $N_B * A_P/A_B$, where A_P is the area of particles ($A_P \sim 0.90$ μm^2). Thus, the vapor pressure can be written as:

$$P_V = \phi_B \, kT/A_P. \qquad [2]$$

From Eq. 1, we can write P_V as:

$$P_V = \phi_C \exp\left(\frac{\Delta\mu}{kT}\right) \frac{kT}{A_P}. \qquad [3]$$

Additionally, by extending the classical nucleation theory (62) to a discrete system, the change in the free energy can be given by:

$$\left(\frac{\Delta G}{\Delta N_C}\right) = 2\pi\gamma\left(\frac{\Delta R}{\Delta N_C}\right) - \frac{\Delta E}{\Delta N_C}, \qquad [4]$$

where γ is the line tension between the bulk and cluster phases, R is the average cluster radius, and ΔE is the energy gained during condensation from bulk to cluster phase. For a cluster,
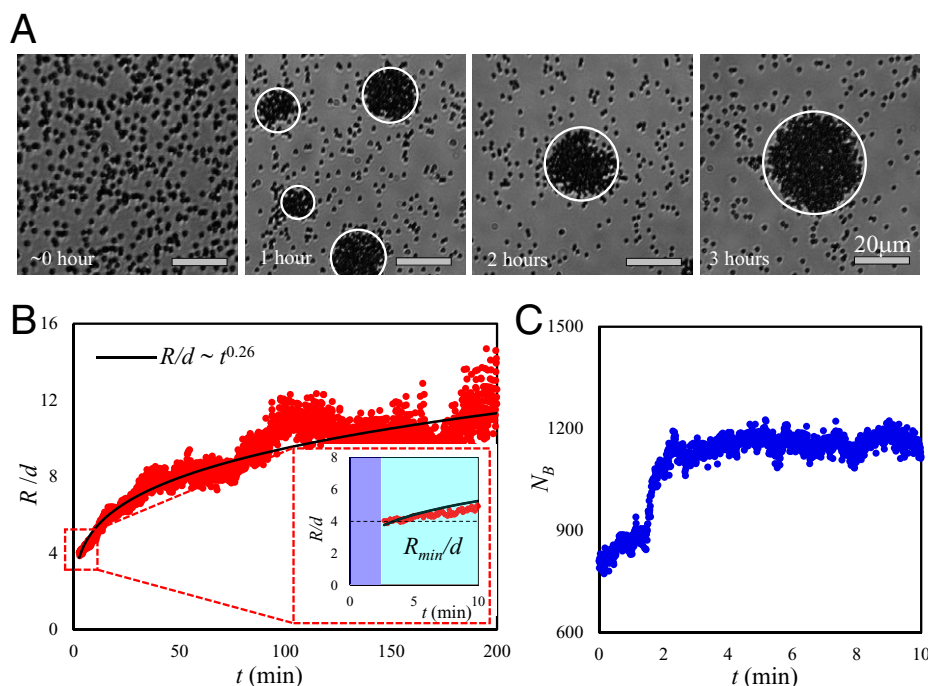
Fig. 2. (*A* and *B*) Coarsening dynamics at 8-G field; the field is turned on at $t = 0$. (*A*) Microscope images at 8G; images were taken at beginning, 1-h, 2-h, and 3-h time scale. (*B*) Coarsening dynamics under RMF. The graph shows average cluster size as a function of time. $R \sim t^{0.26}$. *Inset* shows two regimes upon applied RMF: the system initially goes through nucleation and cluster growth (purple), which is followed by coarsening (aqua). (*C*) Plot showing how the number of bulk particles, N_B, changes when RMF is changed from 9 to 8.5 G; the number of bulk particles N_B were observed. The equilibrium was achieved within a few minutes.

$\Delta R/\Delta N_C$ decreases with an increasing number of particles as $N_C^{-0.5}$. Hence, for larger clusters, $\gamma(\Delta R/\Delta N_C) \to 0$ as the function of magnetic field. Accordingly, the $\Delta G/\Delta N_C$ as a function of the magnetic field is mainly governed by $\Delta E/\Delta N_C$. However, for tiny clusters ($R < R_{min}$), it is difficult to define a constant line tension, as the interface of the cluster constantly fluctuates. Additionally, since $-\Delta E/\Delta N_C \propto kTB^2$ and ϕ_C does not change significantly with the strength of the applied magnetic field, we expect from Eq. 1 that $\ln(\phi_B)$ changes linearly with $\Delta G/\Delta N_C kT \equiv (B^2)$. Lastly, ϕ_B can be correlated with N_B, as shown previously (see *SI Appendix* for details). A representative image of coexistence between the bulk and cluster phases is shown in Fig. 3A, where the bulk particles are identified in blue and the cluster particles in red. The average number of cluster particles is given by $N_C = \langle N_C^i \rangle$, and the average cluster radius is given by the rms of clusters area, $R = \sqrt{\langle (R^i)^2 \rangle}$. Experiments between 10.5 and 8 G were conducted to characterize N_B as a function of RMF strength. The magnetic field was lowered by 0.5 G in a step-wise manner, and at each B, the system was allowed to reach quasi-equilibrium between the bulk and cluster phases. Fig. 3B shows a linear relationship between a normalized N_B (or ϕ_B) as a function B^2. This relates the RMF-driven phase transitions of dipolar colloids to classical thermodynamics. The slope of the plot corresponds to Gibb's free energy for condensation per particle. Thus, $\Delta E/\Delta N_C = 0.046B^2 kT$. Incidentally, this condensation energy is $\sim 2.1\,U_{min}$ (based on Fig. 1A, *Inset*). This is a good estimate for clusters since a perfectly crystalline configuration with six neighbors should have an interaction energy of $3\,U_{min}$. The image stack in Fig. 3C shows N_B and ϕ_B increases as B decreases. Note that the average cluster size remains similar ($R \sim 10d$) for all values of B studied.

Application of Kelvin's Equation to Colloidal Droplets. In this section, we will consider the free-energy changes associated with the cluster size using the value of $\Delta E/\Delta N_C$ obtained from above:

$$\left(\frac{\Delta G}{\Delta N_C}\right) = 2\pi\gamma\left(\frac{\Delta R}{\Delta N_C}\right) - cB^2 kT. \qquad [5]$$
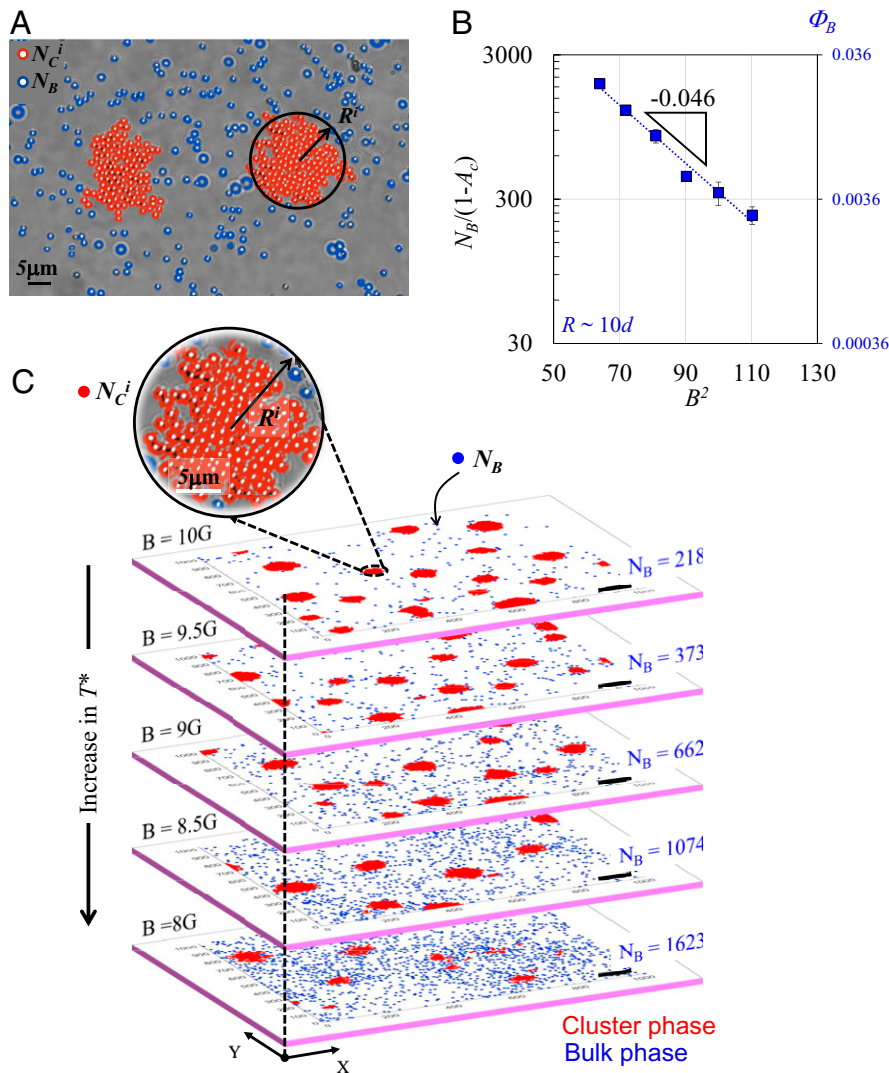

Fig. 3. (A) Microscope image illustrating the equilibrium between particle clusters and the bulk-phase particles. The image obtained at 9 G highlights different variables, such as bulk-phase particles, (N_B), particular cluster particles, (N_C^i), and cluster size, (R^i), as indicated by the black arrow. (B) Bulk particle density as a function of square of magnetic field. The linear relationship validates the analogy to the classical equilibrium model. The slope observed imparts $\Delta E/\Delta N_C = -0.046kTB^2$. (C) Binarized microscopy images illustrate equilibrium between the bulk and cluster phases at varying magnetic fields (effective temperature). The strength of the RMF is varied from 10 to 8 G (top to bottom). Bulk particles are identified in blue and clusters with red color. Note: All the images are (1,024 × 1,024) pixel size.

Here, the energy gained during cluster condensation is written in terms of the applied magnetic field strength, $c = 0.046$. This is only valid for clusters above R_{min}. The radius of the cluster can be written in terms of the cluster particle density and particle diameter, d.

$$R = \left(\frac{d}{2\sqrt{\phi_C}}\right)\sqrt{N_C}. \quad [6]$$

Thus, the free energy can be expressed as:

$$\left(\frac{\Delta G}{\Delta N_C}\right) = \frac{\pi d^2}{4\phi_C}\left(\frac{\gamma}{R}\right) - cB^2 kT. \quad [7]$$

Lastly, this free-energy expression can be substituted into the Boltzmann equation, Eq. 3:

$$P_V = \phi_C \frac{kT}{A_P} \exp(-cB^2) \exp\left(\frac{\pi d^2}{4\phi_C kT}\left(\frac{\gamma}{R}\right)\right). \quad [8]$$

For molecular systems, smaller droplets with corresponding larger curvatures require less energy to remove a molecule from the interface. Since condensation of the bulk phase must equal evaporation at equilibrium, the saturation vapor pressure for small droplets is greater than large droplets. Using this analogy, we define an equilibrium vapor pressure as $P_{Vo} = (\phi_C\, kT/A_P)\, exp(-cB^2)$, which represents the vapor pressure

over a flat bulk–cluster or corresponding vapor–liquid interface. Thus, Eq. 8 can be written as

$$\ln\frac{P_V}{P_{Vo}} = \left(\frac{\pi d^2}{4\phi_C kT}\left(\frac{\gamma}{R}\right)\right). \quad [9]$$

It is important to note that P_{Vo} depends on B, whereas for liquid droplets, the equilibrium vapor pressure over a flat surface depends on T. The value of P_{Vo} for our dipolar system can be approximated by using the spinodal phase, where the interface is close to zero curvature. Our previous work shows that the spinodal phase can be obtained at higher particle densities (42). Fig. 4A shows experimental images taken for three different particle densities, ϕ, identified by $\phi \ni (0.15, 0.18, 0.22)$ with a fixed $B = 8.5$ G. At the highest particle density, the spinodal phase reveals a largely interconnected morphology with relatively flat interfaces. Additionally, although the mean curvature of the spinodal phase averages to zero over the length scale of our system, a finite local curvature is observed. In general, the P_{Vo} represents an asymptotic value of P_V for clusters that increases with R, as is also observed with water droplets (54). At the intermediate particle density, the average cluster radius is $26d$, and at the lowest particle density, the average cluster radius is $10d$. Fig. 4B shows the microscope image of the spinodal phase illustrating the flat interface on a local and wider scale. Fig. 4C gives the relationship between P_V and B^2 for different R. In the graph, blue squares represent $R = 10d$, orange squares represent
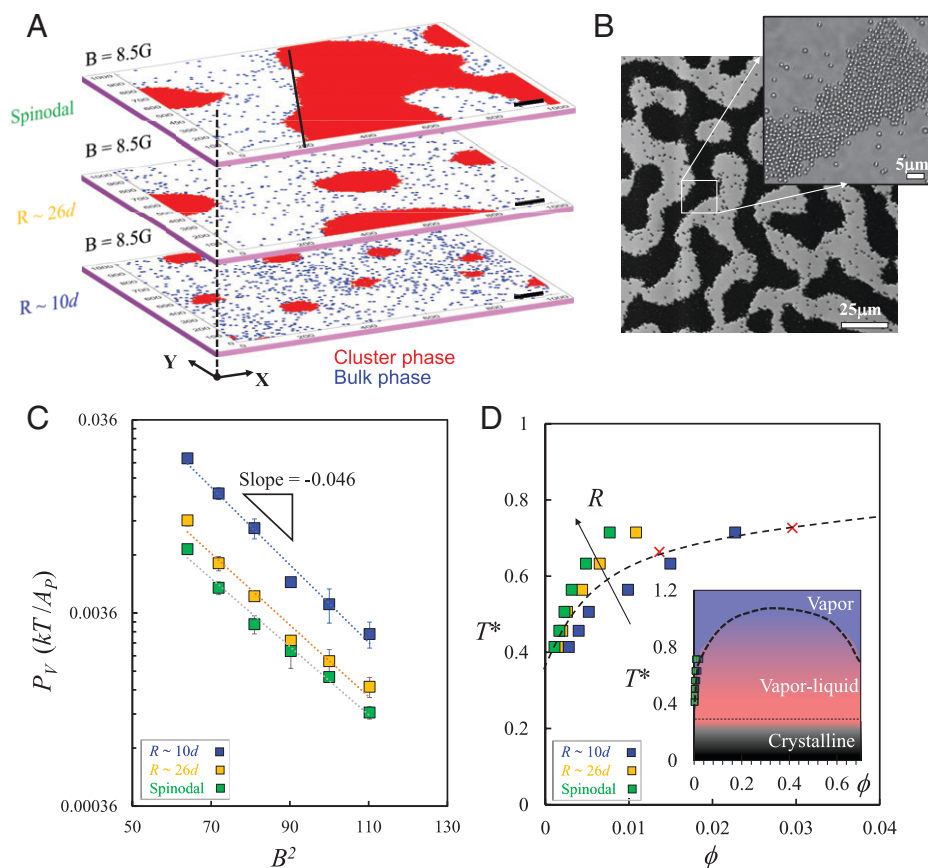

Fig. 4. (A) Experimental images at 8.5 G showing the equilibrium between vapor and liquid phases with different particle area coverage. The morphologies of cluster phase shows different curvatures: *Top*, spinodal; *Middle* and *Bottom*, cluster phase. R represents the average cluster size in micrometers. (B) Microscope image of spinodal morphology illustrating flat interface. *Inset* shows zoomed-in image of flat interface. (C) Graph shows P_V as a function of cluster size and magnetic field. The vapor pressure is expressed in units of kT/A_P. Blue squares, $R = 10d$; orange squares, $R = 26d$; and green squares, $R \approx \infty$. (D) Graph shows $T*$ as a function of ϕ for different R. Blue squares, $R = 10d$; orange squares, $R = 26d$; and green squares, $R \approx \infty$. Dotted line and red crosses represent simulation data previously reported from Kryuchkov et al. (29). *Inset* shows the zoomed-out version of the phase diagram. The ϕ values obtained show good agreement with previous results.

$R = 26d$, and green squares represent the spinodal case $R \approx \infty$. For a given B, the average cluster size governs the P_V as shown in Fig. 4C. This expression also supports the analogy to Kelvin's equation, where the equilibrium vapor pressure over a curved surface increases with decreasing droplet size. Furthermore, the slopes of particle density with magnetic field in Fig. 4C are similar for the three-particle concentrations, confirming that P_V shows a linear trend with B^2 for all cluster sizes. Lastly, P_{Vo} represents the equilibrium vapor pressure over a flat surface, which can be approximated from the results by using the spinodal phase. Fig. 4D shows the $T*$ as a function ϕ on the phase diagram. What can be seen is that our results show good agreement with the computed binodal shown by the dashed line (29). Fig. 4 D, *Inset* highlights the small ϕ values where our vapor pressure is calculated.

Conclusions

In summary, we have shown that Kelvin's equation can be applied to a 2D suspension of superparamagnetic colloids driven to phase-separate into bulk and cluster phases under an RMF, akin to vapor–liquid coexistence. Classical nucleation theory describes homogeneous nucleation of small clusters that grow due to condensation and aggregation to form liquid droplets. This nucleation occurs when the vapor pressure is significantly higher than the equilibrium vapor pressure. The P_v and $T*$ follow a Clausius–Clapeyron relationship as a classical thermal equilibrium between two coexisting phases. Analogously, we have calculated the change in the Gibbs free energy for condensation of bulk colloids at an effective vapor pressure, P_V, into a cluster. Assumptions are made that the colloids in the bulk phase behave as an ideal gas. Additionally, since the colloidal clusters have a curved surface, with curvature $\sim 1/R$, the equilibrium vapor pressure, P_{Vo}, represents that of the flat liquid interface, which we estimated from the spinodal phase. Interestingly, the P_V for our 2D dipolar colloidal clusters depends on the curvature $\sim 1/R$ and follows Kelvin's equation of vapor pressure. At first glance, the results are surprising since Kelvin's equation applies to systems in thermodynamic equilibrium. Gibbs free energy provides the basis for correlating temperature, pressure, and chemical potentials to any well-defined system. Here, the continuous application of the RMF violates the conservation of energy. However, the RMF generated an averaged interaction potential, hence $T*$, connecting back to the classical thermodynamics. With this link, new perspectives to describe the organization and stability of field-driven systems can be made.

1. I. S. Aranson, Collective behavior in out-of-equilibrium colloidal suspensions. *C. R. Phys.* **14**, 518–527 (2013).
2. A. Kaiser, A. Snezhko, I. S. Aranson, Flocking ferromagnetic colloids. *Sci. Adv.* **3**, e1601469 (2017).
3. B. Zhang, A. Sokolov, A. Snezhko, Reconfigurable emergent patterns in active chiral fluids. *Nat. Commun.* **11**, 4401 (2020).
4. A. Yethiraj, A. van Blaaderen, A colloidal model system with an interaction tunable from hard sphere to soft and dipolar. *Nature* **421**, 513–517 (2003).
5. W. F. Paxton *et al.*, Catalytic nanomotors: Autonomous movement of striped nanorods. *J. Am. Chem. Soc.* **126**, 13424–13431 (2004).
6. P. Tierno, R. Golestanian, I. Pagonabarraga, F. Sagués, Magnetically actuated colloidal microswimmers. *J. Phys. Chem. B* **112**, 16525–16528 (2008).
7. R. Dreyfus *et al.*, Microscopic artificial swimmers. *Nature* **437**, 862–865 (2005).
8. T. Yang *et al.*, Reconfigurable microbots folded from simple colloidal chains. *Proc. Natl. Acad. Sci. U.S.A.* **117**, 18186–18193 (2020).
9. A. F. Demirörs, M. T. Akan, E. Poloni, A. R. Studart, Active cargo transport with Janus colloidal shuttles using electric and magnetic fields. *Soft Matter* **14**, 4741–4749 (2018).
10. K. Han *et al.*, Sequence-encoded colloidal origami and microbot assemblies from patchy magnetic cubes. *Sci. Adv.* **3**, e1701108 (2017).
11. Y. Yang, M. A. Bevan, Cargo capture and transport by colloidal swarms. *Sci. Adv.* **6**, eaay7679 (2020).
12. M. Driscoll *et al.*, Unstable fronts and motile structures formed by microrollers. *Nat. Phys.* **13**, 375–379 (2017).
13. V. Soni *et al.*, The odd free surface flows of a colloidal chiral fluid. *Nat. Phys.* **15**, 1188–1194 (2019).
14. R. Evans, D. Frenkel, M. Dijkstra, From simple liquids to colloids and soft matter. *Phys. Today* **72**, 38–39 (2019).
15. W. Poon, Physics. Colloids as big atoms. *Science* **304**, 830–831 (2004).
16. J. Schwarz-Linek *et al.*, Phase separation and rotor self-assembly in active particle suspensions. *Proc. Natl. Acad. Sci. U.S.A.* **109**, 4052–4057 (2012).
17. V. V. Murashov, G. N. Patey, Structure formation in dipolar fluids driven by rotating fields. *J. Chem. Phys.* **112**, 9828–9833 (2000).
18. N. Elsner, C. P. Royall, B. Vincent, D. R. E. Snoswell, Simple models for two-dimensional tunable colloidal crystals in rotating ac electric fields. *J. Chem. Phys.* **130**, 154901 (2009).
19. D. Du, M. Doxastakis, E. Hilou, S. L. Biswal, Two-dimensional melting of colloids with long-range attractive interactions. *Soft Matter* **13**, 1548–1553 (2017).
20. W. Li, X. Qian, J. Li, Phase transitions in 2D materials. *Nat. Rev. Mater.* **6**, 829–846 (2021).
21. P. R. ten Wolde, D. Frenkel, Enhancement of protein crystal nucleation by critical density fluctuations. *Science* **277**, 1975–1978 (1997).
22. V. J. Anderson, H. N. W. Lekkerkerker, Insights into phase transition kinetics from colloid science. *Nature* **416**, 811–815 (2002).
23. C. J. O. Reichhardt, C. Reichhardt, An exceptional view of phase transitions in non-equilibrium systems. *Nature* **592**, 355–356 (2021).
24. S. Jäger, H. Schmidle, S. H. L. Klapp, Nonequilibrium condensation and coarsening of field-driven dipolar colloids. *Phys. Rev. E Stat. Nonlin. Soft Matter Phys.* **86**, 011402 (2012).
25. J. E. Martin, A. Snezhko, Driving self-assembly and emergent dynamics in colloidal suspensions by time-dependent magnetic fields. *Rep. Prog. Phys.* **76**, 126601 (2013).
26. B. Li, X. Xiao, S. Wang, W. Wen, Z. Wang, Real-space mapping of the two-dimensional phase diagrams in attractive colloidal systems. *Phys. Rev. X* **9**, 031032 (2019).
27. N. Osterman *et al.*, Field-induced self-assembly of suspended colloidal membranes. *Phys. Rev. Lett.* **103**, 228301 (2009).
28. A. T. Pham *et al.*, Phase diagram and aggregation dynamics of a monolayer of paramagnetic colloids. *Phys. Rev. E* **95**, 052607 (2017).
29. N. P. Kryuchkov, F. Smallenburg, A. V. Ivlev, S. O. Yurchenko, H. Löwen, Phase diagram of two-dimensional colloids with Yukawa repulsion and dipolar attraction. *J. Chem. Phys.* **150**, 104903 (2019).
30. A. E. Koser, N. C. Keim, P. E. Arratia, Structure and dynamics of self-assembling colloidal monolayers in oscillating magnetic fields. *Phys. Rev. E Stat. Nonlin. Soft Matter Phys.* **88**, 062304 (2013).
31. B. Khusid, A. Acrivos, Phase diagrams of electric-field-induced aggregation in conducting colloidal suspensions. *Phys. Rev. E Stat. Phys. Plasmas Fluids Relat. Interdiscip. Topics* **60**, 3015–3035 (1999).
32. J. A. Wood, A. Docoslis, Electric-field induced phase transitions of dielectric colloids: Impact of multiparticle effects. *J. Appl. Phys.* **111**, 094106 (2012).
33. A. C. H. Coughlan, I. Torres-Díaz, J. Zhang, M. A. Bevan, Non-equilibrium steady-state colloidal assembly dynamics. *J. Chem. Phys.* **150**, 204902 (2019).
34. T. D. Edwards, M. A. Bevan, Controlling colloidal particles with electric fields. *Langmuir* **30**, 10793–10803 (2014).
35. M. Han, J. Yan, S. Granick, E. Luijten, Effective temperature concept evaluated in an active colloid mixture. *Proc. Natl. Acad. Sci. U.S.A.* **114**, 7513–7518 (2017).
36. J. Palacci, C. Cottin-Bizonne, C. Ybert, L. Bocquet, Sedimentation and effective temperature of active colloidal suspensions. *Phys. Rev. Lett.* **105**, 088304 (2010).
37. N. Boon, G. I. Guerrero-García, R. van Roij, M. Olvera de la Cruz, Effective charges and virial pressure of concentrated macroion solutions. *Proc. Natl. Acad. Sci. U.S.A.* **112**, 9242–9246 (2015).
38. B. Jönsson, J. Persello, J. Li, B. Cabane, Equation of state of colloidal dispersions. *Langmuir* **27**, 6606–6614 (2011).
39. E. Hilou, D. Du, S. Kuei, S. L. Biswal, Interfacial energetics of two-dimensional colloidal clusters generated with a tunable anharmonic interaction potential. *Phys. Rev. Mater.* **2**, 025602 (2018).
40. M. Santra, B. Bagchi, Line tension of a two dimensional gas-liquid interface. *J. Chem. Phys.* **131**, 084705 (2009).
41. E. H. A. de Hoog, H. N. W. Lekkerkerker, Measurement of the interfacial tension of a phase-separated colloid-polymer suspension. *J. Phys. Chem. B* **103**, 5274–5279 (1999).
42. E. Hilou, K. Joshi, S. L. Biswal, Characterizing the spatiotemporal evolution of paramagnetic colloids in time-varying magnetic fields with Minkowski functionals. *Soft Matter* **16**, 8799–8805 (2020).
43. S. Jäger, S. H. L. Klapp, Pattern formation of dipolar colloids in rotating fields: Layering and synchronization. *Soft Matter* **7**, 6606 (2011).
44. P. Tierno, R. Muruganathan, T. M. Fischer, Viscoelasticity of dynamically self-assembled paramagnetic colloidal clusters. *Phys. Rev. Lett.* **98**, 028301 (2007).
45. S. C. Takatori, J. F. Brady, Towards a thermodynamics of active matter. *Phys. Rev. E Stat. Nonlin. Soft Matter Phys.* **91**, 032117 (2015).
46. G. S. Redner, C. G. Wagner, A. Baskaran, M. F. Hagan, Classical nucleation theory description of active colloid assembly. *Phys. Rev. Lett.* **117**, 148002 (2016).
47. S. Paliwal, V. Prymidis, L. Filion, M. Dijkstra, Non-equilibrium surface tension of the vapour-liquid interface of active Lennard-Jones particles. *J. Chem. Phys.* **147**, 084902 (2017).
48. Y. Fily, M. C. Marchetti, Athermal phase separation of self-propelled particles with no alignment. *Phys. Rev. Lett.* **108**, 235702 (2012).

49. R. Wittkowski et al., Scalar $\phi 4$ field theory for active-particle phase separation. *Nat. Commun.* **5**, 4351 (2014).
50. S. C. Takatori, W. Yan, J. F. Brady, Swim pressure: Stress generation in active matter. *Phys. Rev. Lett.* **113**, 028103 (2014).
51. A. P. Solon et al., Pressure and phase equilibria in interacting active Brownian spheres. *Phys. Rev. Lett.* **114**, 198301 (2015).
52. V. Prymidis, S. Samin, L. Filion, State behaviour and dynamics of self-propelled Brownian squares: A simulation study. *Soft Matter* **12**, 4309–4317 (2016).
53. F. Ginot et al., Nonequilibrium equation of state in suspensions of active colloids. *Phys. Rev. X* **5**, 011004 (2015).
54. M. H. Factorovich, V. Molinero, D. A. Scherlis, Vapor pressure of water nanodroplets. *J. Am. Chem. Soc.* **136**, 4508–4514 (2014).
55. D. Du, D. Li, M. Thakur, S. L. Biswal, Generating an in situ tunable interaction potential for probing 2-D colloidal phase behavior. *Soft Matter* **9**, 6867 (2013).
56. M. Tagliazucchi, E. A. Weiss, I. Szleifer, Dissipative self-assembly of particles interacting through time-oscillatory potentials. *Proc. Natl. Acad. Sci. U.S.A.* **111**, 9751–9756 (2014).
57. C. Udink, D. Frenkel, Orientational order and solid-liquid coexistence in the two-dimensional Lennard-Jones system. *Phys. Rev. B Condens. Matter* **35**, 6933–6939 (1987).
58. B. Smit, D. Frenkel, Vapor–liquid equilibria of the two-dimensional Lennard-Jones fluid(s). *J. Chem. Phys.* **94**, 5663–5668 (1991).
59. S. Ranganathan, G. S. Dubey, K. N. Pathak, Molecular-dynamics study of two-dimensional Lennard-Jones fluids. *Phys. Rev. A* **45**, 5793–5797 (1992).
60. H. Schmidle, C. K. Hall, O. D. Velev, S. H. L. Klapp, Phase diagram of two-dimensional systems of dipole-like colloids. *Soft Matter* **8**, 1521–1531 (2012).
61. P. V. Ovcharov, N. P. Kryuchkov, K. I. Zaytsev, S. O. Yurchenko, Particle-resolved phase identification in two-dimensional condensable systems. *J. Phys. Chem. C* **121**, 26860–26868 (2017).
62. V. D. Nguyen, F. C. Schoemaker, E. M. Blokhuis, P. Schall, Measurement of the curvature-dependent surface tension in nucleating colloidal liquids. *Phys. Rev. Lett.* **121**, 246102 (2018).

ENGINEERING